applied sciences

MDPI

Article

Enhanced μCT Imaging Protocol to Enable High-Resolution 3D Visualization of Microdamage in Rat Vertebrae

Allison Tolgyesi [1,2], Normand Robert [1], Cari M. Whyne [1,2,3,*] and Michael Hardisty [1,3]

[1] Orthopaedic Biomechanics Laboratory, Sunnybrook Research Institute, Toronto, ON M4N 3M5, Canada
[2] Institute of Biomedical Engineering, University of Toronto, Toronto, ON M5S 3G9, Canada
[3] Division of Orthopaedics, Department of Surgery, University of Toronto, Toronto, ON M5T 1P5, Canada
* Correspondence: cwhyne@sri.utoronto.ca

Featured Application: The following work suggests enhanced μCT image acquisition parameters for high-resolution visualization of barium sulfate contrast in bone samples for use in investigations of microdamage in three dimensions.

Abstract: Contrast-enhanced μCT imaging has been used to provide non-destructive 3D images of microdamage, but at a lower quality than found in histology and 2D backscatter electron (BSE) imaging. This study aimed to quantify potential improvements in microdamage characterization by enhancing μCT scanning parameters. Eleven slides from 9 rat vertebrae (healthy = 3, osteolytic metastases = 3, mixed metastases = 3) previously stained for microdamage with $BaSO_4$ and analyzed with BSE imaging (2μm voxel spacing) were used in this study. μCT imaging conducted under varying protocols (x-ray voltage, tube current, frame averaging) demonstrated enhanced scan parameters at 90 kVp, 44 μA, 0.5 mm aluminum filter, 8 times frame averaging, and 4.9 μm voxel spacing. Post-processing with Richardson-Lucy deconvolution further deblurred the μCT images. Labeled microdamage in the baseline, enhanced and deblurred μCT images were segmented and spatially quantified vs. BSE-labeled microdamage using a probability-based correlation metric at six inflation radii. Enhanced μCT scan parameters improved damage visualization and increased spatial correlation probability with BSE images. Deblurring improved the sharpness of stain boundaries but did not significantly improve spatial correlation probabilities in comparison to the enhanced scans. This enhanced μCT protocol facilitates 3D visualization of microdamage, an indicator of bone quality important to bone damage mechanics.

Keywords: bone; micro-computed tomography (μCT); microdamage; spatial correlation

Citation: Tolgyesi, A.; Robert, N.; Whyne, C.M.; Hardisty, M. Enhanced μCT Imaging Protocol to Enable High-Resolution 3D Visualization of Microdamage in Rat Vertebrae. *Appl. Sci.* **2023**, *13*, 3625. https://doi.org/10.3390/app13063625

Academic Editor: Marco Giannelli

Received: 18 February 2023
Revised: 8 March 2023
Accepted: 10 March 2023
Published: 12 March 2023

1. Introduction

Microcracks and damage occur in bone during normal use, with damage playing a role in regulating bone turnover. Homeostasis in the healthy bone between osteoblastic and osteoclastic cell activity maintains bone integrity, replacing damaged bone tissue and adjusting the bone shape to mechanical loading. Diseases (cancer, osteoporosis) or treatment (bisphosphonates, radiation) are known to affect damage distribution by affecting bone turnover or bone material properties [1–4]. Skeletal microdamage has previously been studied with two-dimensional (2D) histological analyses, including light microscopy with basic fuchsin staining [5–7] or chelating fluorochromes [8]. Backscatter electron (BSE) microscopy with lead-uranyl acetate [9] or barium sulfate ($BaSO_4$) stain [10–12] has also been used for high-resolution 2D imaging of skeletal microdamage, with the difference in atomic number between the labeling stain and the bony matrix providing excellent contrast for identifying damaged regions within bone tissue. While histologic analyses are the most common method of quantifying microdamage, both histology and BSE are destructive techniques limited to 2D analysis.

Distinct from optical microscopes, scanning electron microscopes (SEMs) use electrons (rather than light) to produce images of specimens. BSEs are high-energy electrons that are reflected out of the specimen during SEM imaging that highlight the different elements contained in the specimen. Denser elements (those with a high atomic number) deflect incident electrons more strongly than lighter elements, thus appearing brighter in a BSE image acquired with an SEM [13]. This characteristic of BSE images allows for the study of mineralization in bone tissue, as regions high in hydroxyapatite (a mineral composed of calcium, phosphate, and hydroxide) appear bright. Visualizing high atomic number contrast agents is facilitated by BSE imaging as the bright contrast may be easily located and segmented from the images. SEM imaging acquires images under a vacuum. Thus, specimens must be dehydrated, or a cryo-fixation technique must be employed [13,14]. Bones' inorganic phase and relatively low water content compared to soft biological tissues allow for the dehydration method without the need for the more complicated cryo-fixation. The dehydration process, however, requires weeks of progressive dehydration to limit artifacts (microcracks) induced by drying [13]. As the surface topology of the samples must be flat, bone specimens require embedding in resin and subsequent surface polishing. This can further induce artifacts and requires additional time for resin polymerization [13]. To avoid static charge buildup on the sample surface, non-conductive samples such as bone must be rendered conductive. Strategies to achieve this include impregnation of the sample with heavy metals, applying a thin conductive coating (such as carbon), or use of ionic liquids [13].

Computed tomography is a non-invasive imaging tool providing three-dimensional (3D) images of biological structures. Micro-computed tomography (μCT) allows for high-resolution images on a smaller scale, which has value for pre-clinical studies of biological tissues. μCT leverages the varying x-ray attenuations of biological tissues to generate images [15]. As the sample is rotated inside the μCT scanner (or the detector is rotated around the specimen), the intensity of x-rays transmitted through the tissues at different angles is measured by the detector [15,16]. The collection of 2D projections is then reconstructed post-acquisition to create the 3D image using a process called back-projection [15]. As the intensity of tissues in μCT images is determined by radiodensity (the relative inability of x-rays to pass through a material), μCT is best suited for distinguishing different types of tissues, such as bone versus muscle. The use of radiopaque contrast agents allows for otherwise undetectable structures (vasculature, bone microdamage) to be visualized with μCT imaging [16,17]. Images acquired with μCT can be acquired in as little as 20 min to 12 h depending on the sample size, desired voxel spacing, and image resolution. Biological samples may also remain hydrated and intact, as μCT scans are acquired at atmospheric pressure.

μCT image quality is determined by the image acquisition parameters and reconstruction algorithm employed by the scanner but may further be improved with post-image acquisition techniques. μCT images inherently contain spatial blurring, which can be quantified by a point spread function (PSF) [18–20]. The PSF defines image resolution and is the result of blurring induced by the finite size of the focal spot size, the x-ray detector aperture (the spatial resolution of the detector itself) [21], and the scattering of x-rays [22]. Spatial blurring may result in thin bone features (such as trabeculae) having a diffuse appearance, which overestimates their thickness and underestimates their intensity. For microstructural analyses of bone, this may negatively affect the quality of results. The localization and quantification of contrast agents may additionally be disrupted, as blurring may reduce their intensity. The application of deconvolution algorithms, which act to reduce blurring and noise, may correct the PSF to render images more closely to their true representations.

Non-destructive 3D assessment of damage is possible via μCT imaging with radiopaque contrast agents. Previous investigators have studied 3D skeletal microdamage distribution using μCT imaging of $BaSO_4$-labeled bovine and rodent bone [12,23,24]. Microdamage accumulation found in μCT images of $BaSO_4$-labeled human cortical bone cores has been strongly correlated with histologic crack density but with more variability [10]. BSE imaging of $BaSO_4$-labeled rodent vertebrae [25] has been shown to yield superior

visualization of microcracks and crack nucleation surfaces compared to high-resolution μCT imaging.

Trabecular bone contains a fine structure of mineralized tissue with individual strut thickness that can vary from 25–1000 μm. Microdamage and cracks present within trabecular bone are on the order of microns to millimeters. As such, μCT-based microdamage assessments in trabecular bone are highly dependent on image acquisition parameters and the imaging system, given the overlap of resolution possible with μCT and the structures being imaged. This study aims to enhance μCT-based microdamage characterization in rat vertebrae labeled with $BaSO_4$ contrast by careful consideration of the x-ray physics (k-edge x-ray adsorption), physical specimen size, limitations of μCT systems (focal spot size interaction with tube current and voltage), and post-acquisition enhancement (deblurring) [18,26], and compare patterns of microdamage visualized with μCT to BSE imaging.

2. Materials and Methods

2.1. Sample Generation

This protocol was approved by the animal care committee at the University Health Network prior to implementation. Healthy (n = 3) and metastatically involved (osteolytic (n = 3) mixed osteolytic/osteoblastic (n = 3)) athymic female rat vertebrae generated from previous work were used in this study [25]. The rodent model for the physiological development of vertebral metastases in immunocompromised rats was established previously [27–30]. Briefly, 5–6-week-old athymic female rats were randomly assigned to healthy, osteolytic metastatic, or mixed osteolytic/osteoblastic metastatic groups. Osteolytic or mixed metastases were generated with HeLa human cervical cancer cells or canine Ace-1 prostate cancer cells, respectively. The animals were anesthetized with nose-cone inhalation of a 2% isoflurane/air mixture, and ~1.5×10^6 cells (in 0.2 mL of Dulbecco's modified eagle medium/nutrient mixture F-12 media) were injected into the left heart ventricle. The animals were euthanized 21 days after cell injection *via* CO_2 asphyxiation, and the T12-L2 vertebral motion segments were separated, wrapped in saline-soaked gauze, and stored at −20 °C until use. These healthy and metastatically involved vertebrae provide a wide range with respect to the presence of microdamage accumulation. T13-L2 spinal motion segments were stained with 0.5 M barium chloride followed by 0.5 M sodium sulfate solution, each for 72 h, under vacuum [10]. Microdamage was induced in the L1 vertebra under axial compressive loading (50 N held for 3 h) with a loading rate of 35 μm/s. The L1 vertebrae were separated and re-stained with $BaSO_4$ post-loading to label load-induced microdamage [25,31]. Staining was repeated in [17] to correlate load-induced microdamage with stresses and strains calculated with micro-finite element models. However, the method described here is focused solely on correlating $BaSO_4$ distribution across imaging modalities. The post-loaded specimens were used in the analyses to maximize the amount of damage present in the bone.

2.2. Backscatter Electron Imaging and Baseline μCT Imaging

Previous work prepared the L1 vertebrae for BSE imaging by fixing the samples in 2% paraformaldehyde and dehydrating them in rising concentrations of ethanol immersed in an osteo-bed kit [25]. The sample blocks were polymerized, secured to a slide with epoxy, cut in the sagittal plane with a water-cooled precision diamond saw (Isomet® low-speed saw, Buehler, Lake Bluff, IL, USA), and polished with increasing grits of silicon carbide paper and diamond paste. Slides of the sagittal cross-sections of hard-embedded L1 vertebrae were carbon-coated, and BSE images were acquired at ×150 magnification with 2 μm/pixel spacing (SS BSE detector, FEI, Hillsboro, OR, USA) using a Philips XL30 ESEM (FEI). Eleven BSE slides (healthy = 5, osteolytic = 3, mixed = 3) were μCT imaged (μCT-100, Scanco Medical, Brüttisellen, Switzerland) at baseline scan parameters (55 kVp, 200 μA, 0.5 mm Al filter, 250 ms integration time, no frame averaging, 11.4 μm voxel spacing) [25]. Image processing of the BSE and μCT images to quantify microdamage is described in Section 2.4.

2.3. Enhanced μCT Imaging

These 11 slides prepared for BSE imaging were re-imaged with parameters selected to maximize contrast between $BaSO_4$ and bone, also considering voxel spacing, resolution, and signal-to-noise ratio (SNR). SNR is proportional to the square root of the products of current, integration time, and frame averaging. The contrast between $BaSO_4$ and bone is enhanced by maximizing the relative energy contribution of x-ray photons having energy just above the 37.4 keV k-edge of barium. The peak of the x-ray photon energy spectrum as a function of x-ray energy occurs at ~1/3 of the tube voltage value. Selecting a tube voltage of 90 kVp, the maximum available, will therefore increase the fraction of x-ray photons with energy just below the k-edge of barium, maximizing contrast. By the same logic, the attenuation of lower energy photons also improves contrast and can be achieved by using an attenuating material with a sufficiently high atomic number such that photoelectric x-ray absorption becomes the dominant absorption process. Photoelectric absorption is more pronounced at lower photon energy, thereby removing the undesired lower energy photons. Thus, the 0.5 mm aluminum filter (1 of 3 options) used in the baseline scans sufficiently reduces the contribution of lower energy photons, reducing soft tissue contrast and beam hardening. This filter is suitable to be added to the x-ray beam for an enhanced set of image acquisition parameters.

Reconstruction voxel spacing requirements are governed by the size of details of interest but must also consider computation limitations like processing time, memory, and storage, limiting the number of voxels. The image resolution should also be commensurate with voxel spacing, as storing a blurry image with a small pixel spacing is wasteful. The specification of smaller reconstructed voxel spacings limits the maximum sample holder diameter because the μCT uses geometric magnification, trading off the field of view to increase resolution at the detector. In this application, a voxel spacing of 4.9 μm (1 of 7 choices) was chosen with the sample holder of 14 mm inner diameter, the maximum value having an x-ray projection that can be encompassed by the detector.

A higher x-ray tube current creates more x-ray photons per unit time, thereby increasing the SNR achievable per unit time of imaging. This requires a larger x-ray focal spot so as not to damage the x-ray anode due to excessive energy deposition density, increasing x-ray projection blurring at the detector. The tube current was thus limited to a value of 44 μA (1 of 5 choices available), so the associated (dependent) focal spot size does not cause noticeable blurring.

Finally, the process of analyzing images and comparing modalities require μCT images with a minimum SNR, which depends on the square root of the number of detected x-ray photons for a given x-ray spectrum. This number, for a given x-ray tube current, is proportional to the amount of time that the x-ray detector collects radiation and is also known as the integration time [32,33]. The Scanco μCT-100 additionally allows several images to be acquired at each projection angle and combined, a process labeled as frame averaging. Thus, the number of detected x-ray photons used to image a sample with a 2000 ms integration time and no averaging is the same as imaging with a 250 ms integration time and 8 times frame averaging. The former approach will, however, lead to a faster scan time. Frame averaging is useful when SNR requirements cannot be achieved by increasing the integration time alone. In these experiments, we chose to only vary frame averaging for descriptive simplicity. The SNR was evaluated by examining images with the above-specified parameters; frame averaging was increased up to 8 times to improve the SNR to offset limitations encountered with the use of low current. Note: frame averaging greatly increases the scan time, which may not always be practical depending on the type and number of samples to be analyzed.

The x-ray beam is sufficiently penetrating that no spectral adjustments (kVp, filtration) are required to compensate for limited attenuation differences of the samples of interest due to variations in extent and morphology. Compensations for said changes in attenuation can be achieved by varying the total x-ray exposure time and/or tube current alone. Larger

x-ray focal spots associated with larger tube currents might be tolerable if the larger sample is also imaged with a larger voxel spacing, so blurring is not noticeable.

Semi-quantitative evaluation criteria focused on maximum contrast between the $BaSO_4$ and bone without saturation, sharpness of trabecular bone boundaries, presence of artifacts (beam hardening, scatter, noise), and graininess of the images to tune the μCT image acquisition parameters.

2.4. Image Processing and Deblurring Algorithm

μCT images were cropped to only include five slices from the top face of the BSE slides to facilitate comparison and reduce computational expense [34]. 3D Slicer software (3D Slicer 4.8.1) was used to transform, resample, and register the five μCT slices and individual BSE images of each sample. A single μCT plane was extracted from registration with the BSE image. Registration error was measured using fiducials placed on paired BSE and μCT images. Five fiducials were placed on all image pairs, and the distance between fiducials was averaged for each sample.

An established deblurring algorithm (based on Richardson-Lucy deconvolution) was applied to the enhanced μCT images [18,26]. The PSF was modeled as a Gaussian and using a custom module (https://bitbucket.org/OrthopaedicBiomechanicsLab/deblurring, accessed on 20 October 2020), the in- and out-of-plane blurring were estimated by placing profiles (implemented as rulers) across thin regions of cortical bone. Profile locations were chosen as thin cortical bone structures with non-bone regions on both sides (air or marrow) such that there were three distinct layers, or greyscale values, across the profile. In-plane blurring was estimated by profiles placed in the sagittal plane, and out-of-plane blurring was estimated by profiles placed in the coronal and axial planes. Theoretical PSF should be equal in identically acquired images (same μCT scanner using the same parameters). Thus, an average was calculated based on the estimated in-plane blurring in each image (0.0067 ± 0.0007 mm). Due to their thinness (~500 μm), the slides did not have enough visible structures in the coronal and axial directions to estimate out-of-plane blurring. A whole fresh frozen vertebra (age-matched, identical HeLa cell injection protocol) was μCT imaged with the enhanced scan parameters. Out-of-plane blurring was estimated from this image as 0.0068 mm. All enhanced μCT images were deblurred using the average in-plane and single out-of-plane blurring parameters as inputs to the Richardson-Lucy deconvolution algorithm.

The $BaSO_4$ contrast was segmented from the μCT (baseline, enhanced (Figure 1a), and deblurred) and BSE images (3D Slicer segmentation editor). First, the whole bone was segmented with automated thresholding using the Otsu method [35–37]. The segmentation was shrunk by 50 μm from the outer edge (Figure 1b, light green) of the cortical shell to remove non-specific contrast not caused by microdamage [10,11]. $BaSO_4$ was segmented inside the shrunken label field (Figure 1c, light blue) using thresholding at a greyscale intensity of 253 for the BSE images and ~2500 mgHA/cm^3 for the μCT images. The BSE images were 8-bit images with no intensity calibration for $BaSO_4$. As the difference in density between barium and calcium is high, and the greyscale intensity bins are limited to the 8-bit range for the BSE images, the pixel intensities corresponding to $BaSO_4$ were concentrated around the upper intensities of the image. As such, pixel intensities of 253 or above were sufficient in segmenting $BaSO_4$ from the BSE images.

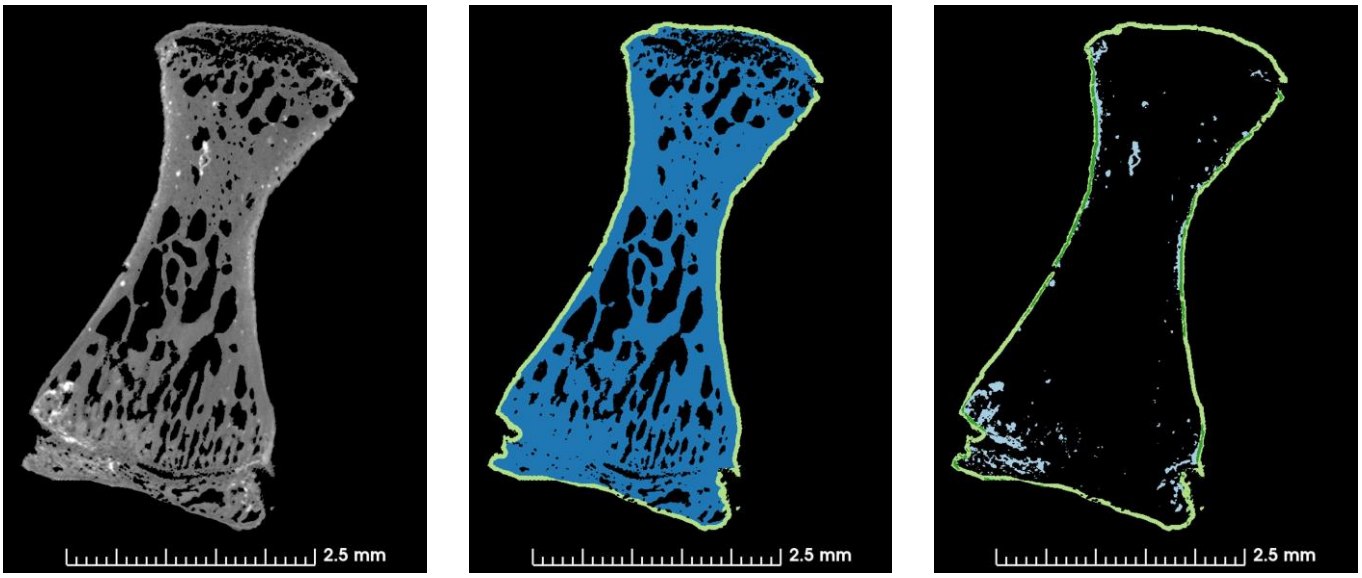

(**a**) (**b**) (**c**)

Figure 1. Stain segmentation procedure on an enhanced μCT image. (**a**) unlabeled enhanced μCT image with background removed; (**b**) bone label field (blue) less than 50 μm of the outer edge of the cortical shell (light green); (**c**) labeled $BaSO_4$ (light blue) used for damage volume fraction calculations and showing excluded $BaSO_4$ contrast (green).

2.5. Spatial Correlation

The spatial correlation between labeled microdamage in paired BSE and μCT images (i.e., from the same sample) was determined using a probability-based method [38,39]. All calculations and comparisons were performed within image pairs. For each sample, there were four imaging modalities: baseline μCT parameters, enhanced μCT parameters, enhanced μCT parameters with deblurring, and BSE imaging. The probability of observing labeled microdamage in a μCT image within some radius of labeled microdamage in a BSE image was determined for all labeled voxels. Additionally, the probability of observing labeled microdamage in a BSE image within some radius of labeled microdamage in a μCT image was determined. Probabilities were calculated at radii of 0, 10, 20, 30, 40, 50, and 60 μm from labeled pixels, chosen based on the trabecular thickness and the μCT spatial resolution. To demonstrate, Figure 2 shows the label fields used for the probability of spatial correlation calculations at a 30 μm radius between a BSE and enhanced μCT image. To model varying radii considered as correlated, $BaSO_4$ labeled pixels in one image (i.e., the BSE image in Figure 2a, the enhanced μCT image in Figure 2b) was "inflated" using convolution with circular kernels with radii of 10–60 μm. The probability of observing spatially close pixels was calculated as the relative number of intersecting $BaSO_4$-labeled pixels in paired images. As the inflation radius increases, more pixels in the inflated image are labeled as $BaSO_4$, thus increasing the likelihood that a $BaSO_4$-labeled pixel in the non-inflated image will intersect. The probability is calculated twice for each pair to ensure mutual correlation. Figure 2a shows the label fields used to calculate the probability that $BaSO_4$-labeled pixels in an enhanced μCT image fall within 30 μm of $BaSO_4$-labeled pixels in a BSE image. Figure 2b shows the label fields used to calculate the probability for the opposite direction, namely that $BaSO_4$-labeled pixels in a BSE image fall within 30 μm of $BaSO_4$-labeled pixels in an enhanced μCT image.

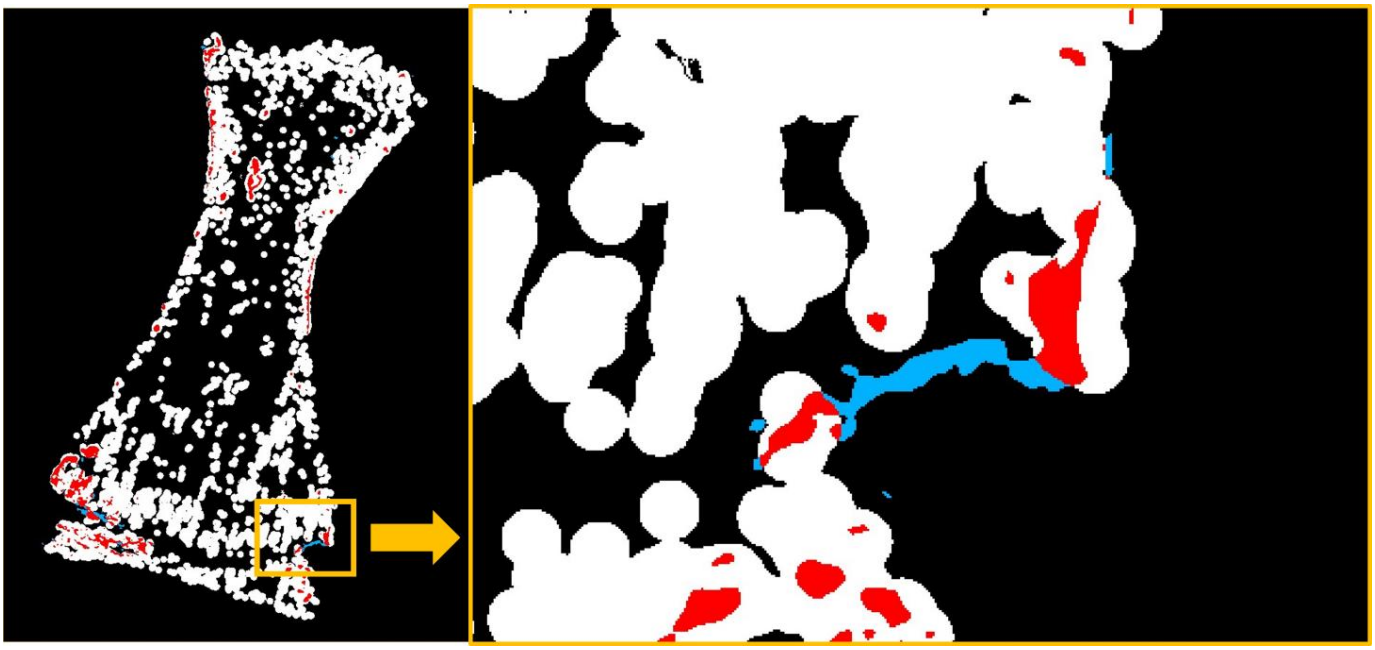

(**a**)

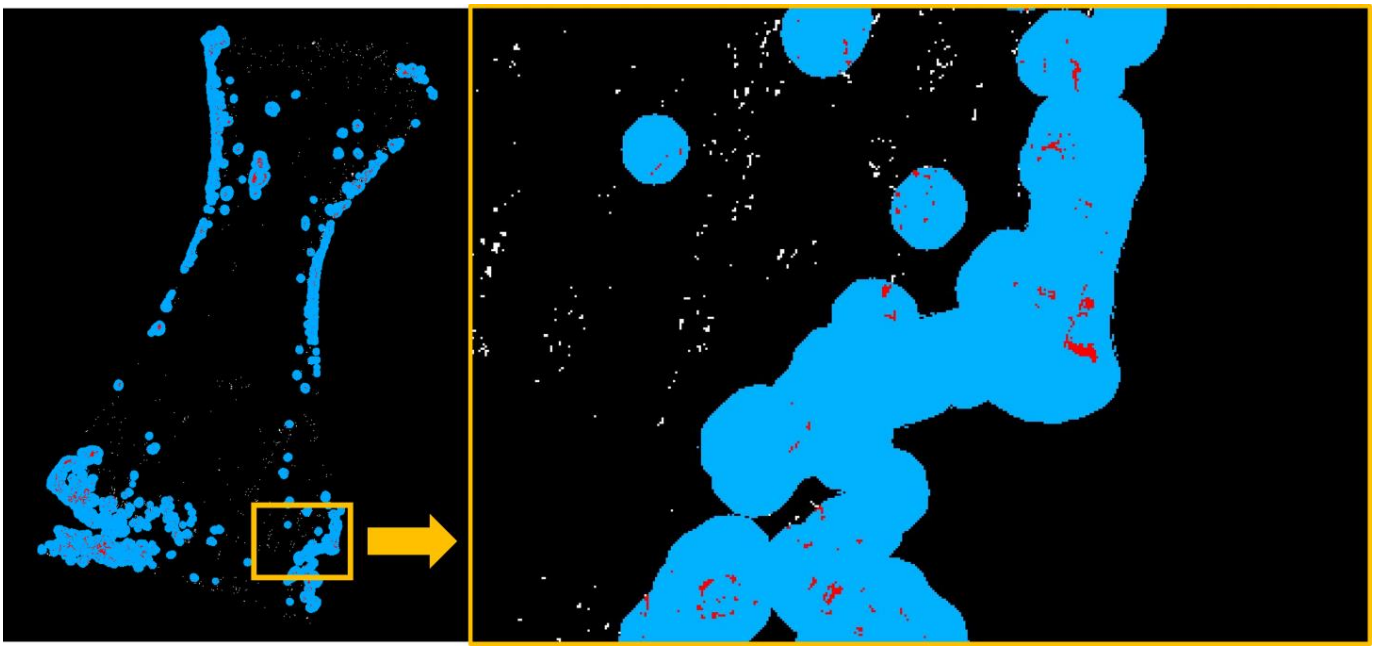

(**b**)

Figure 2. Label fields used to calculate spatial correlation probability of $BaSO_4$-labeled pixels between BSE and enhanced µCT images at an inflation radius of 30 µm. (**a**) the probability of $BaSO_4$-labeled pixels in an enhanced µCT image (blue) being within 30 µm of $BaSO_4$-labeled pixels in an inflated BSE image (white). The probability of spatial correlation is calculated as the ratio of red to blue pixels. (**b**) the probability of $BaSO_4$-labeled pixels in a BSE image (white) being within 30 µm of $BaSO_4$-labeled pixels in an inflated enhanced µCT image (blue). Red areas represent overlapping $BaSO_4$-labeled pixels in both images. The probability of spatial correlation is calculated as the ratio of red to white pixels.

Damage area fraction (DAF) was defined as the ratio of intersecting bone and $BaSO_4$ pixels to bone pixels, described in Equation (1):

$$DAF = \frac{\#\left(p_{BaSO_4} \cap p_{bone}\right)}{\#p_{bone}} \quad (1)$$

where p_{BaSO_4} is the set of all $BaSO_4$-labeled pixels and p_{bone} is the set of all bone-labeled pixels. DAF was calculated for every modality after each convolution for inflation.

2.6. Statistical Analysis

Measures of DAF exhibited non-normal residual distributions; therefore, a Friedman non-parametric test was used with sample number as a random effect. Post-hoc comparisons were performed using the Nemenyi test (RStudio). Mean microdamage correlation probability in both correlation directions (BSE to μCT and μCT to BSE) was compared between image pair groups with a two-way ANOVA with sample number as a random effect. Tukey pairwise post-hoc comparisons were performed between each image pair at each radius. The level of significance for all tests was set at 0.05.

3. Results

3.1. Enhanced μCT Imaging and Deblurring

Varying currents (all other parameters fixed, 70 kVp, no frame averaging) demonstrated that lower currents improved the visualization of trabecular edges. Increasing frame averaging using a fixed low current improved the SNR. Increased voltage improved the contrast between $BaSO_4$ and bone while maintaining low current and high frame averaging. Tuned μCT parameters (90 kVp, 44 μA, 0.5 mm Al filter, 200 ms integration time, 8 frame averaging, 4.9 μm voxel spacing) enhanced visualization of the damaged regions compared to the baseline μCT scan parameters. Table 1 shows a summary of the baseline and enhanced μCT acquisition parameters. The current was kept low enough for the tube to operate with a small focal spot size to yield sharp images. Due to the limitations with respect to the current, frame averaging was increased to improve damage visualization. Each scan took 2.1 h collecting images for a volume of ~500 μm in height. The enhanced μCT images show microdamage that is obscured by reduced resolution and low contrast in the baseline μCT images (Figure 3). The deblurring algorithm visually sharpened the regions of the $BaSO_4$ contrast agent seen in the enhanced μCT images and identified smaller areas of $BaSO_4$ not picked up in the enhanced image. The mean registration error between paired BSE and μCT images (baseline, enhanced, deblurred) was 0.01 ± 0.008 mm.

Table 1. Summary of μCT acquisition parameters for baseline and enhanced protocols for visualization of $BaSO_4$-labeled microdamage in rat vertebral bone.

Acquisition Protocol	Voltage (kVp)	Tube Current (μA)	Filter	Integration Time (ms)	Frame Averaging	Voxel Spacing (μm)
Baseline	55	200	0.5 mm Al	250	N/A	11.4
Enhanced	90	44	0.5 mm Al	200	8	4.9

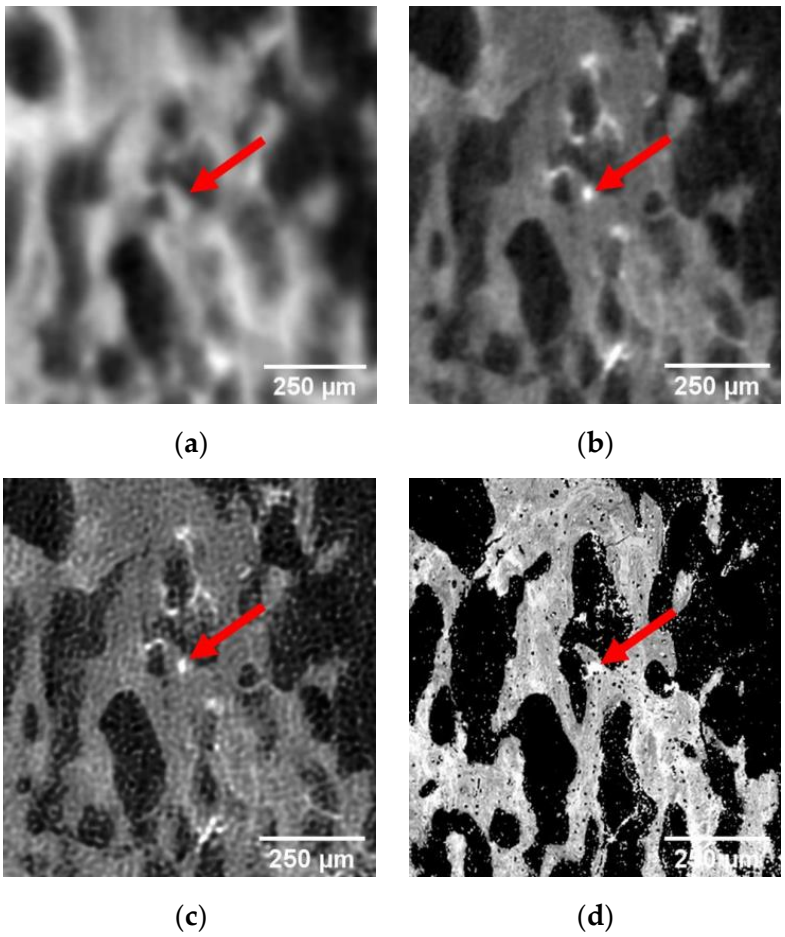

Figure 3. $BaSO_4$ visualization of microdamage in trabecular bone of a healthy rat L1 vertebra with four imaging modalities. (**a**) baseline µCT; (**b**) enhanced µCT; (**c**) enhanced µCT with a deblurring algorithm applied post-acquisition; (**d**) BSE imaging. The red arrow identified matching *$BaSO_4$* stained structures in all images.

3.2. Damage Area Fraction

DAF in all image types increased with inflation radius (Figure 4). Uninflated (radius = 0 µm), DAF in the baseline µCT scans is significantly higher than the enhanced and BSE images ($p = 0.026$, $p < 0.001$, respectively). However, for every non-zero inflation radius, the BSE and deblurred µCT images have significantly higher DAFs than the baseline and enhanced images.

Convolving (or inflating) the *$BaSO_4$*-labeled pixels blur the damage, which increases the area identified as *$BaSO_4$*. Higher stain areas are measured on the BSE images when there is inflation as smaller areas of *$BaSO_4$*-labeled pixels are connected, forming larger regions. In µCT images, more of the *$BaSO_4$*-labeled pixels are clumped in regions representing larger areas of damage; pixels inflated at the center of a clump do not contribute to additional stain.

While DAF is equal across the enhanced, deblurred, and BSE images without inflation, the deblurred and BSE images likely identify smaller areas of stain and estimate smaller areas for concentrated *$BaSO_4$* clumps than the enhanced images.

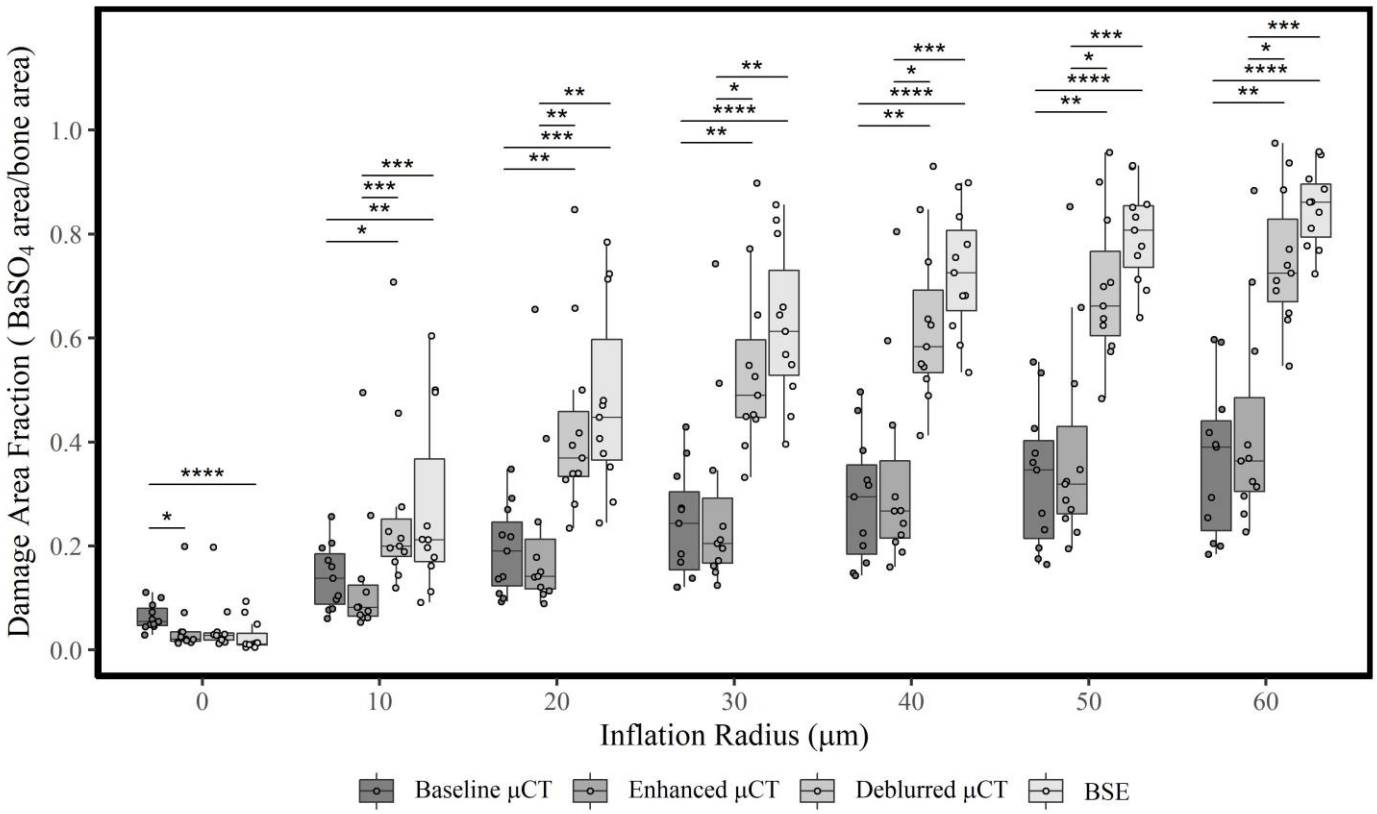

Figure 4. Damage area fractions ($BaSO_4$ area/bone area) of $BaSO_4$ label fields in μCT and BSE images before (radius = 0 μm) and after convolution inflating the label fields at six radii. The data represented are from eleven sagittal BSE slides from rat L1 vertebrae (healthy = 5, osteolytic = 3, mixed = 3). * $p < 0.05$, ** $p < 0.01$, *** $p < 0.001$, **** $p < 0.0001$, Nemenyi pair-wise comparison.

3.3. Damage Spatial Correlation

Considering both directions of probability calculations, the enhanced and deblurred μCT imaging showed a greater spatial correlation of damage with BSE than the baseline μCT imaging (BSE-labeled damage occurring near μCT labeled damage and vice versa). As expected, spatial correlation probability between image pairs (BSE and baseline μCT, BSE and enhanced μCT, BSE and deblurred μCT) increased with larger inflation radii (Figure 5). Post-hoc pairwise comparison showed the probability of finding $BaSO_4$-labeled pixels in enhanced μCT images near $BaSO_4$-labeled pixels in BSE images was significantly greater than in the baseline μCT images for inflation radii of 10–40 μm ($p = 0.0002$–0.045, Figure 5a). When BSE images were inflated (Figure 5a), the deblurring algorithm showed no significant differences compared to enhanced μCT at any inflation radii ($p = 0.32$–0.99). The probability of spatial correlation approached 1 when the BSE images were inflated (Figure 5a), as the DAF of BSE images also approached 1 (due to the inflation of many small, distributed pixels throughout the specimens), increasing the likelihood of finding a μCT pixel in this area.

The probability of finding a $BaSO_4$-labeled pixel in a BSE image spatially close to one in a μCT image was significantly different for each μCT modality at all inflation radii. Post-hoc pairwise comparison showed the deblurring algorithm to have the highest probability of spatial correlation compared to baseline and enhanced images at all inflation radii ($p < 0.0001$–0.002, Figure 5b). For both directions, there were no significant differences across μCT modalities when no convolution was applied ($p = 0.082$–0.99, radius = 0 μm).

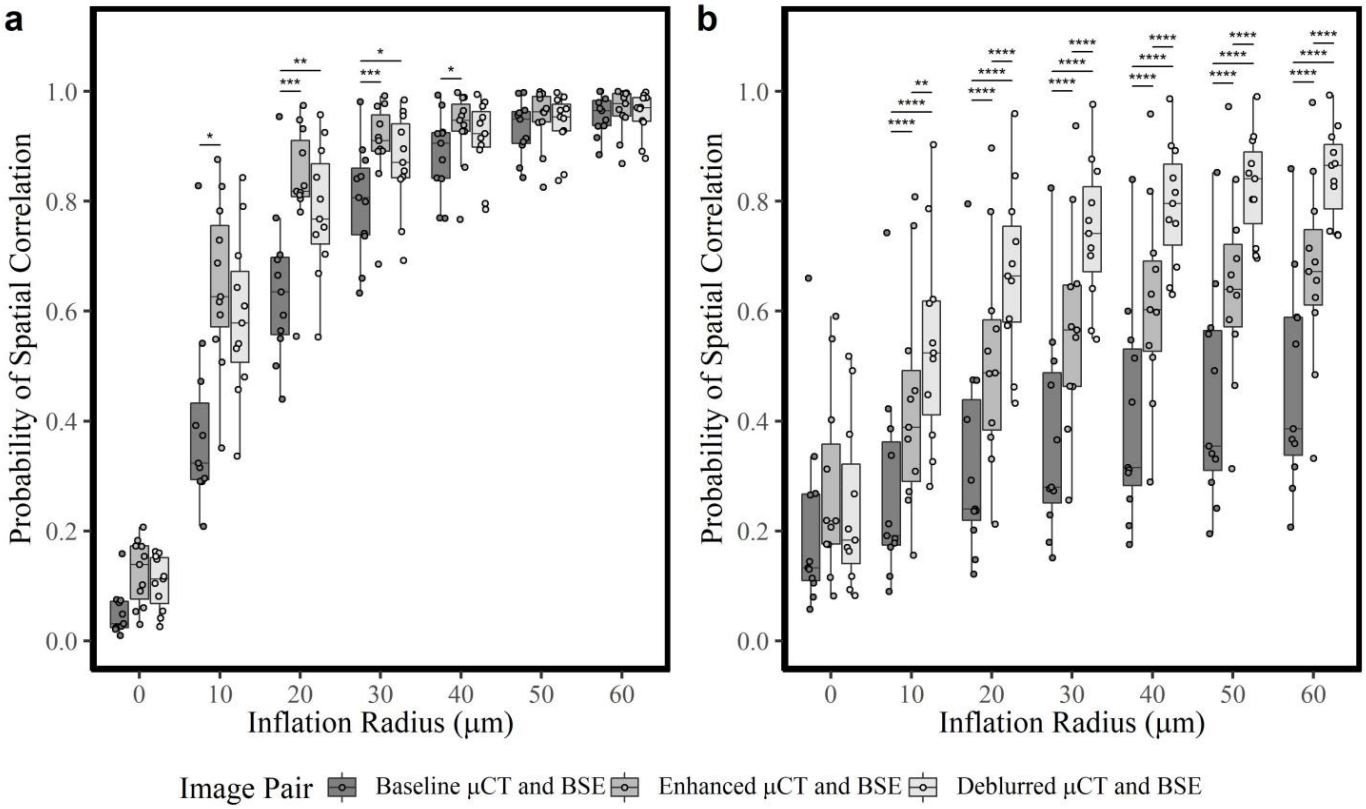

Figure 5. Probability of spatial correlation of $BaSO_4$-labeled pixels in paired μCT (baseline, enhanced, and deblurred) and BSE images at six inflation radii. (**a**) the probability that $BaSO_4$-labeled pixels in a μCT image (baseline, enhanced, or deblurred) fall within some radius of $BaSO_4$-labeled pixels in a BSE image; (**b**) the probability that $BaSO_4$-labeled pixels in a BSE image fall within some radius of $BaSO_4$-labeled pixels in a μCT image (baseline, enhanced, or deblurred). The data presented are from eleven sagittal BSE slides from rat L1 vertebrae (healthy = 5, osteolytic = 3, mixed = 3). * $p < 0.05$, ** $p < 0.01$, *** $p < 0.001$, **** $p < 0.0001$, Tukey pair-wise comparison.

4. Discussion

Enhancements to μCT scanning parameters and deblurring post-acquisition both qualitatively and quantitatively improved visualization of damage deposition. Enhanced parameter voxel spacing of 4.9 μm represents higher resolution imaging than historically used for 3D microdamage analysis with $BaSO_4$ labeling [10,25]. Visualization of microdamage with this μCT protocol is dependent on the efficacy of the $BaSO_4$ staining (ability to precipitate into all microdamage sites). This is an important consideration, as contrary to BSE imaging, the enhanced μCT parameters are not able to distinguish microdamage that is not labeled by the $BaSO_4$ contrast. $BaSO_4$ labels all damage types (microfractures, diffuse damage, linear microcracks), limiting the specificity of damage characterization by intensity alone; the enhanced techniques presented in this investigation potentially allow the examination of morphology to determine the damage type. Effective assessment of damage distribution in 3D allows for the study of how damage interacts with remodeling, prediction of failure, and treatment responses.

This investigation studied trabeculae with thicknesses of 75–95 μm and spacing of 90–126 μm [25], which may explain the lack of difference between the enhanced techniques and baseline μCT imaging at larger inflation radii (Figure 5a). Our tuning of μCT acquisition parameters was limited by pre-set voltage and current combinations available on the scanner, preventing any determination if higher voltage could further increase the contrast between bone and $BaSO_4$. Spatial correlation accuracy was impacted by registration errors between BSE and μCT image pairs, limiting the strength of findings at the smaller inflation

radii. Frame averaging and small voxel spacing in the enhanced scan parameters resulted in long scan times and large file sizes for whole rat vertebrae (~11 h, ~8 GB for ~1500 slices), which is not suitable for samples without fixation. The deblurring algorithm requires extensive computational resources that may be unavailable for total volume deblurring using the enhanced parameters.

Eight times frame averaging is a major contributor to increased scan acquisition time in this protocol. However, the reduced noise in these images facilitates the segmentation of small $BaSO_4$-labeled regions. Increasing integration time may have further reduced noise, however, at the expense of greater scan acquisition times when combined with eight times averaging. Thus, this study did not investigate the magnitude of noise reduction when increasing integration time and frame averaging concurrently. While the acquisition time is long, the process for obtaining BSE images is extensive, requiring weeks for sample dehydration and hard embedding (5 weeks total for the BSE slides used in this study). The enhanced μCT protocol allows results to be obtained by the next day, is non-destructive to the sample, and provides 3D spatial location and distribution of damage. Scan acquisition time and file size prevents the enhanced μCT parameters outlined in this protocol from being used for the microdamage analysis of whole bones from large mammals or humans. However, bone cores (trabecular and cortical) are often used to study microdamage distribution in larger bone samples [10,35,40,41], which would be feasible for this protocol.

5. Conclusions

Enhancing μCT protocols provides high-resolution visualization of $BaSO_4$-labeled microdamage that spatially locates $BaSO_4$ near BSE-identified microdamage. 3D visualization of microdamage allows global observation of accumulation and distribution, which could influence further crack propagation and potential fracture locations. The use of a deblurring algorithm may be beneficial but may not be practical for high-resolution μCT scans because of the significant computational expense. Further research regarding factors affecting microdamage accumulation and its influence on bone material properties, including fracture behavior, can be facilitated with this protocol.

Author Contributions: Conceptualization, C.M.W. and M.H.; methodology, A.T. and N.R.; formal analysis, A.T. and N.R.; investigation, A.T.; resources, C.M.W.; data curation, A.T.; writing—original draft preparation, A.T.; writing—review and editing, N.R., C.M.W. and M.H.; visualization, A.T.; supervision, C.M.W. and M.H.; project administration, C.M.W. and M.H.; funding acquisition, C.M.W. All authors have read and agreed to the published version of the manuscript.

Funding: This research was funded by the Canadian Institutes of Health Research, grant number 156175, and the Canadian Graduate Scholarships—Master's, the Ontario Graduate Scholarship, and the Feldberg Chair for Spinal Research.

Institutional Review Board Statement: The animal study protocol was approved by the animal care committee at the University Health Network prior to implementation (AUP 6044.10, 14 September 2021).

Informed Consent Statement: Not applicable.

Data Availability Statement: No new data were created or analyzed in this study. Rat vertebrae were acquired from work published previously. Data sharing is, therefore, not applicable to this article.

Conflicts of Interest: The authors declare no conflict of interest.

References

1. Allen, M.R.; Burr, D.B. Bisphosphonate Effects on Bone Turnover, Microdamage, and Mechanical Properties: What We Think We Know and What We Know That We Don't Know. *Bone* **2011**, *49*, 56–65. [CrossRef] [PubMed]
2. Mashiba, T.; Hirano, T.; Turner, C.H.; Forwood, M.R.; Johnston, C.C.; Burr, D.B. Suppressed Bone Turnover by Bisphosphonates Increases Microdamage Accumulation and Reduces Some Biomechanical Properties in Dog Rib. *J. Bone Miner. Res.* **2000**, *15*, 613–620. [CrossRef] [PubMed]
3. Allen, M.R.; Burr, D.B. Skeletal Microdamage: Less about Biomechanics and More about Remodeling. *Clin. Rev. Bone Miner. Metab.* **2008**, *6*, 24–30. [CrossRef]

4. Mashiba, T.; Turner, C.H.; Hirano, T.; Forwood, M.R.; Johnston, C.C.; Burr, D.B. Effects of Suppressed Bone Turnover by Bisphosphonates on Microdamage Accumulation and Biomechanical Properties in Clinically Relevant Skeletal Sites in Beagles. *Bone* **2001**, *28*, 524–531. [CrossRef] [PubMed]
5. Burr, D.B.; Stafford, T. Validity of the Bulk-Staining Technique to Separate Artifactual from in Vivo Bone Microdamage. *Clin. Orthop. Relat. Res.* **1990**, *260*, 305–308. [CrossRef]
6. Frost, H. Presence of Microscopic Cracks in Vivo in Bone. *Henry Ford Hosp. Med. J.* **1960**, *8*, 25.
7. Lee, T.C.; Myers, E.R.; Hayes, W.C. Fluorescence-Aided Detection of Microdamage in Compact Bone. *J. Anat.* **1998**, *193*, 179–184. [CrossRef] [PubMed]
8. Lee, T.C.; Arthur, T.L.; Gibson, L.J.; Hayes, W.C. Sequential Labelling of Microdamage in Bone Using Chelating Agents. *J. Orthop. Res.* **2000**, *18*, 322–325. [CrossRef] [PubMed]
9. Schaffler, M.B.; Pitchford, W.C.; Choi, K.; Riddle, J.M. Examination of Compact Bone Microdamage Using Back-Scattered Electron Microscopy. *Bone* **1994**, *15*, 483–488. [CrossRef]
10. Landrigan, M.D.; Li, J.; Turnbull, T.L.; Burr, D.B.; Niebur, G.L.; Roeder, R.K. Contrast-Enhanced Micro-Computed Tomography of Fatigue Microdamage Accumulation in Human Cortical Bone. *Bone* **2011**, *48*, 443–450. [CrossRef]
11. Turnbull, T.L.; Baumann, A.P.; Roeder, R.K. Fatigue Microcracks That Initiate Fracture Are Located near Elevated Intracortical Porosity but Not Elevated Mineralization. *J. Biomech.* **2014**, *47*, 3135–3142. [CrossRef]
12. Turnbull, T.L.; Gargac, J.A.; Niebur, G.L.; Roeder, R.K. Detection of Fatigue Microdamage in Whole Rat Femora Using Contrast-Enhanced Micro-Computed Tomography. *J. Biomech.* **2011**, *44*, 2395–2400. [CrossRef]
13. Shah, F.A.; Ruscsák, K.; Palmquist, A. 50 Years of Scanning Electron Microscopy of Bone—A Comprehensive Overview of the Important Discoveries Made and Insights Gained Into Bone Material Properties in Health, Disease, and Taphonomy. *Bone Res.* **2019**, *7*, 15. [CrossRef]
14. Scharf, D. Viewing and Recording Live Hydrated Specimens with a High-Vacuum SEM. *Micros. Today* **2017**, *25*, 12–17. [CrossRef]
15. Boerckel, J.D.; Mason, D.E.; McDermott, A.M.; Alsberg, E. Microcomputed Tomography: Approaches and Applications in Bioengineering. *Stem Cell Res. Ther.* **2014**, *5*, 144. [CrossRef]
16. Bentley, M.D.; Ortiz, M.C.; Ritman, E.L.; Romero, J.C. The Use of Microcomputed Tomography to Study Microvasculature in Small Rodents. *Am. J. Physiol. Regul. Integr. Comp. Physiol.* **2002**, *282*, R1267–R1279. [CrossRef]
17. Guldberg, R.E.; Ballock, R.T.; Boyan, B.D.; Duvall, C.L.; Lin, A.S.P.; Nagaraja, S.; Oest, M.; Phillips, J.; Porter, B.D.; Robertson, G.; et al. Analyzing Bone, Blood Vessels, and Biomaterials with Microcomputed Tomography. *IEEE Eng. Med. Biol. Mag.* **2003**, *22*, 77–83. [CrossRef]
18. Pakdel, A.; Robert, N.; Fialkov, J.; Maloul, A.; Whyne, C. Generalized Method for Computation of True Thickness and X-ray Intensity Information in Highly Blurred Sub-Millimeter Bone Features in Clinical CT Images. *Phys. Med. Biol.* **2012**, *57*, 8099–8116. [CrossRef] [PubMed]
19. Maloul, A.; Fialkov, J.; Whyne, C. The Impact of Voxel Size-Based Inaccuracies on the Mechanical Behavior of Thin Bone Structures. *Ann. Biomed. Eng.* **2011**, *39*, 1092–1100. [CrossRef] [PubMed]
20. Treece, G.M.; Gee, A.H.; Mayhew, P.M.; Poole, K.E.S. High Resolution Cortical Bone Thickness Measurement from Clinical CT Data. *Med. Image Anal.* **2010**, *14*, 276–290. [CrossRef] [PubMed]
21. Pelc, N.J. Recent and Future Directions in CT Imaging. *Ann. Biomed. Eng.* **2014**, *42*, 260–268. [CrossRef]
22. Hsieh, J. *Computed Tomography: Principles, Design, Artifacts, and Recent Advances*, 2nd ed.; John Wiley & Sons, Ltd.: Hoboken, NJ, USA, 2009; ISBN 9780819480422.
23. Leng, H.; Wang, X.; Ross, R.D.; Niebur, G.L.; Roeder, R.K. Micro-Computed Tomography of Fatigue Microdamage in Cortical Bone Using a Barium Sulfate Contrast Agent. *J. Mech. Behav. Biomed. Mater.* **2008**, *1*, 68–75. [CrossRef] [PubMed]
24. Wang, X.; Masse, D.B.; Leng, H.; Hess, K.P.; Ross, R.D.; Roeder, R.K.; Niebur, G.L. Detection of Trabecular Bone Microdamage by Micro-Computed Tomography. *J. Biomech.* **2007**, *40*, 3397–3403. [CrossRef]
25. Atkins, A.; Burke, M.; Samiezadeh, S.; Akens, M.K.; Hardisty, M.; Whyne, C.M. Elevated Microdamage Spatially Correlates with Stress in Metastatic Vertebrae. *Ann. Biomed. Eng.* **2019**, *47*, 980–989. [CrossRef] [PubMed]
26. Pakdel, A.; Mainprize, J.G.; Robert, N.; Fialkov, J.; Whyne, C.M. Model-Based PSF and MTF Estimation and Validation from Skeletal Clinical CT Images. *Med. Phys.* **2014**, *41*, 011906. [CrossRef]
27. Engebraaten, O.; Fodstad, Ø. Site-Specific Experimental Metastasis Patterns of Two Human. *Int. J. Cancer* **1999**, *82*, 219–225. [CrossRef]
28. Lo, V.C.K.; Akens, M.K.; Wise-Milestone, L.; Yee, A.J.M.; Wilson, B.C.; Whyne, C.M. The Benefits of Photodynamic Therapy on Vertebral Bone Are Maintained and Enhanced by Combination Treatment with Bisphosphonates and Radiation Therapy. *J. Orthop. Res.* **2013**, *31*, 1398–1405. [CrossRef]
29. Hojjat, S.P.; Won, E.; Hardisty, M.R.; Akens, M.K.; Wise-Milestone, L.M.; Whyne, C.M. Non-Destructive Evaluation of the Effects of Combined Bisphosphonate and Photodynamic Therapy on Bone Strain in Metastatic Vertebrae Using Image Registration. *Ann. Biomed. Eng.* **2011**, *39*, 2816–2822. [CrossRef] [PubMed]
30. Won, E.; Wise-Milestone, L.; Akens, M.K.; Burch, S.; Yee, A.J.M.; Wilson, B.C.; Whyne, C.M. Beyond Bisphosphonates: Photodynamic Therapy Structurally Augments Metastatically Involved Vertebrae and Destroys Tumor Tissue. *Breast Cancer Res. Treat.* **2010**, *124*, 111–119. [CrossRef] [PubMed]

31. Herblum, R.; Beek, M.; Whyne, C.M. MFEA Successfully Exhibits Higher Stresses and Strains in Microdamaged Regions of Whole Vertebrae. *J. Orthop. Res.* **2013**, *31*, 1653–1660. [CrossRef] [PubMed]
32. Bouxsein, M.L.; Boyd, S.K.; Christiansen, B.A.; Guldberg, R.E.; Jepsen, K.J.; Müller, R. Guidelines for Assessment of Bone Microstructure in Rodents Using Micro-Computed Tomography. *J. Bone Miner. Res.* **2010**, *25*, 1468–1486. [CrossRef]
33. Kim, Y.; Brodt, M.D.; Tang, S.Y.; Silva, M.J. MicroCT for Scanning and Analysis of Mouse Bones. In *Skeletal Development and Repair: Methods and Protocols*; Hilton, M.J., Ed.; Springer: New York, NY, USA, 2021; pp. 169–198, ISBN 978-1-0716-1028-2.
34. Fedorov, A.; Beichel, R.; Kalpathy-Cramer, J.; Finet, J.; Fillion-Robin, J.C.; Pujol, S.; Bauer, C.; Jennings, D.; Fennessy, F.; Sonka, M.; et al. 3D Slicer as an Image Computing Platform for the Quantitative Imaging Network. *Magn. Reson. Imaging* **2012**, *30*, 1323–1341. [CrossRef]
35. Goff, M.G.; Lambers, F.M.; Sorna, R.M.; Keaveny, T.M.; Hernandez, C.J. Finite Element Models Predict the Location of Microdamage in Cancellous Bone Following Uniaxial Loading. *J. Biomech.* **2015**, *48*, 4142–4148. [CrossRef]
36. Goff, M.G.; Lambers, F.M.; Nguyen, T.M.; Sung, J.; Rimnac, C.M.; Hernandez, C.J. Fatigue-Induced Microdamage in Cancellous Bone Occurs Distant from Resorption Cavities and Trabecular Surfaces. *Bone* **2015**, *79*, 8–14. [CrossRef] [PubMed]
37. Otsu, N. A Threshold Selection Method from Gray-Level Histograms. *IEEE Trans. Syst. Man. Cybern.* **1979**, *9*, 62–66. [CrossRef]
38. Cresswell, E.N.; Goff, M.G.; Nguyen, T.M.; Lee, W.X.; Hernandez, C.J. Spatial Relationships between Bone Formation and Mechanical Stress within Cancellous Bone. *J. Biomech.* **2016**, *49*, 222–228. [CrossRef]
39. Schulte, F.A.; Ruffoni, D.; Lambers, F.M.; Christen, D.; Webster, D.J.; Kuhn, G.; Müller, R. Local Mechanical Stimuli Regulate Bone Formation and Resorption in Mice at the Tissue Level. *PLoS ONE* **2013**, *8*, e62172. [CrossRef] [PubMed]
40. Lambers, F.M.; Bouman, A.R.; Tkachenko, E.V.; Keaveny, T.M.; Hernandez, C.J. The Effects of Tensile-Compressive Loading Mode and Microarchitecture on Microdamage in Human Vertebral Cancellous Bone. *J. Biomech.* **2014**, *47*, 3605–3612. [CrossRef] [PubMed]
41. Lambers, F.M.; Bouman, A.R.; Rimnac, C.M.; Hernandez, C.J. Microdamage Caused by Fatigue Loading in Human Cancellous Bone: Relationship to Reductions in Bone Biomechanical Performance. *PLoS ONE* **2013**, *8*, e83662. [CrossRef]